Available online at www.sciencedirect.com
ScienceDirect
Trans. Nonferrous Met. Soc. China 28(2018) 1582−1592
Transactions of Nonferrous Metals Society of China
www.tnmsc.cn

Evaluation of $LaAlO_3$ as top coat material for thermal barrier coatings

N. VOURDAS[1], E. MARATHONITI[1], P. K. PANDIS[1],
Chr. ARGIRUSIS[2], G. SOURKOUNI[3], C. LEGROS[4], S. MIRZA[5], V. N. STATHOPOULOS[1]

1. Laboratory of Chemistry and Materials Technology, School of Technological Applications, Technological Educational Institute of Sterea Ellada, 34400 Psachna Campus, Evia, Greece;
2. School of Chemical Engineering, National Technical University of Athens, I. Polytechneiou 9, 15780 Zografou, Athens, Greece;
3. Inst. f. Metallurgie, Technische Universität Clausthal, Robert-Koch-Str. 42, 38678 Clausthal-Zellerfeld, Germany;
4. Institut de Chimie Moléculaire et des Materiaux d´Orsay, Université Paris Sud, Bât 410, 91405 Orsay Cedex, France;
5. ELEMENT S.A., Hitchin SG4 0TW, UK

Received 8 May 2017; accepted 4 August 2017

Abstract: Perovskite is a versatile group of oxide materials allowing their properties to be tailored by composition towards specific requirements. $LaAlO_3$ was prepared to study and report its properties in the context of its potential in thermal barrier coatings (TBCs) technology. A citric acid method was used for synthesis and the perovskite structure was confirmed using XRD and FT-IR. Viscosity of the solution precursor was checked as well as the particle size by laser particle size analysis. Densification behavior of the material was followed by conventional sintering and by spark plasma sintering. Apparent porosity by the Archimedes method, thermal conductivity and thermal expansion coefficient were studied. Mechanical and fracture properties were measured at elevated temperatures up to 1300 °C. For samples sintered at 1200−1400 °C, coefficient of thermal expansion ranged from 5.5×10^{-6} to 6.5×10^{-6} K^{-1} and thermal conductivity ranged between 2.2 and 3.4 W/(m·K). Elastic modulus and ultimate stress were measured at 1000−1300 °C, while by micro-indentation, fracture toughness was found to be 3 $MPa\cdot m^{1/2}$. As the sintering temperature increased from 1200 to 1500 °C, significant densification from 3.21 to 5.81 g/cm^3 was found, indicating that material annealing should be made at least at 1400 °C. Under this condition, negligible dimensional change in phase transition temperature of $LaAlO_3$ from the rhombohedral (*R*3*c*) to the ideal cubic (*Pm*3*m*) is found. Data reported in this work can be useful for comparing the mechanical and fracture behaviours of different TBCs developed involving $LaAlO_3$ as well as input for numerical simulations.
Key words: perovskite; lanthanum aluminate; thermal barrier coating (TBC)

1 Introduction

Thermal barrier coatings (TBCs) are used to insulate and protect the metallic gas turbine engine components from the hot gas stream, against high temperature corrosion, and subsequent damage. Improvement in this field will facilitate higher combustion temperatures and thus improved engine efficiency, not only in power generation but also in aerospace and marine propulsion [1−6]. In general, a typical TBC consists of two deposited layers, the bondcoat (BC) and the topcoat (TC), and one that is evolved during processing and operation, the thermal grown oxide (TGO).

The state of the art TC material is the Y_2O_3-stabilized zirconia (7% Y_2O_3 in ZrO_2, YSZ). This particular Y_2O_3 percentage was selected based on thermal cycling measurements [5]. Its comparably higher thermal cycling performance is leveraged by a combination of suitable properties, i.e., high melting point 2680 °C, high coefficient of thermal expansion (CTE) 11.5×10^{-6} K^{-1} at 1000 °C, low thermal conductivity (*K*) 2.12 W/(m·K) at 1000 °C and high fracture toughness 1−2 $MPa\cdot m^{1/2}$ of the coating [6,7]. YSZ performance is affected by a variety of interconnected parameters, such as the compatibility with the BC material, the BC/TC interface state, the microstructure and the deposition method. However, YSZ operation temperature is limited at ~1200 °C, above which the phase transformation to the monoclinic phase becomes favourable. This transformation introduces fatal

Corresponding author: V. N. STATHOPOULOS; Tel: +30-2228099688; Fax: +30-2228023766; E-mail: vasta@teiste.gr
DOI: 10.1016/S1003-6326(18)64800-9

volume changes that degrade the integrity upon thermal cycling, thus inseminating the necessity for studies of novel TC materials operating at temperatures above 1200 °C [1,8−15].

Materials exhibiting perovskite structure, in particular, have attracted much attention as YSZ replacements mainly due to their high melting point, high CTE and relatively low thermal conductivity. The drawback of materials exhibiting simple perovskite structure is mainly their inferior fracture-related mechanical properties. $SrZrO_3$ is one of the few exceptions with comparable to YSZ fracture toughness and has been studied as single layer TC [16,17] or as double layer on top of YSZ [18], with or without Gd_2O_3 or Yb_2O_3 doping to lower the thermal conductivity and improve the phase stability. Other simple perovskite structured zirconates such as $BaZrO_3$ [16] and $CaZrO_3$ [19] and $LaYbO_3$ [20] have been also evaluated, but their poor thermo-chemical stability and low melting point, respectively, prevail their application as YSZ replacements. $MgZrO_3$ has been used as a buffer layer between YSZ and BC to enhance the damage resistance of the TBC [21]. Nanocomposite materials such as $LaAlO_3$−$La_2Zr_2O_7$, $LaAlO_3$−$LaCuAl_{11}O_{19}$ have been studied as overlayers on YSZ and exhibited improved thermal cycling performance [22]. Simple perovskite structured aluminates have attracted less attention.

An important aspect of perovskites, however, is that they may accommodate substitution in both *A*- and *B*-site, thus allowing their properties to be tailored towards specific requirements as for example in catalysis [23−28]. Under the concept of compositional control of properties, and based on the structures previously synthesized for various applications, complex substituted structures have been studied as YSZ replacements; $Ba(Mg_{1/3}Ta_{2/3})O_3$ (BMT) with CTE=10.9×10^{-6} K^{-1} and k=2.71 W/(m·K) and $La(Al_{1/4}Mg_{1/2}Ta_{1/4})O_3$ (LAMT) with CTE=9.7×10^{-6} K^{-1} and k=1.82 W/(m·K) [29] (CTE values within the range of 30−1000 °C, and k at 1000 °C) have been synthesized and evaluated as one layer TC or as double layer TC on YSZ [11]. Even though their fracture toughness is lower compared with YSZ, and their performance at operating temperatures of 1400 °C is characterized as encouraging. However, the presence of Mg introduces implications upon spraying [30] due to relatively high vapor pressure of MgO (order of 133.3×10^{-4} Pa at 1300 °C), compared Ta_2O_5 (order of 133.3×10^{-4} Pa at 1920 °C), to Al_2O_3 (order of 133.3×10^{-4} Pa at 1550 °C) and to La_2O_3 (133.3×10^{-4} Pa at 1400 °C).

Even though $LaAlO_3$ is claimed as a potential YSZ replacement [31,32], no pertaining study has been published so far to our knowledge, contrary to the respective substituted lanthanum aluminates exhibiting the hexaaluminate structure [33,34]. Even in hexa-aluminates, as well as in lanthanum zirconates [35,36], $LaAlO_3$ gradually evolves with thermal aging [34], due to the reaction of La with Al from the evolved TGO. More interestingly, La oxide seems to stabilize the sintering and hence the creep resistance of Al oxide [37]. Therefore, its evaluation as material incorporated in the TC of a TBC, is of crucial importance not only as stand-alone TC layer, but also for various La-containing YSZ replacements including nanocomposites [22].

Simple $LaAlO_3$ structure demonstrates poor mechanical properties [38], which has a relatively low melting point (ca. 2100 °C), and exhibits a phase transition from the rhombohedral (*R*3*c*) to the ideal cubic (*Pm*3*m*) at ca. 810−840 °C, accompanied with a CTE discontinuity. The extent of this discontinuity is however debatable, from prohibitively large [39,40] to undistinguishable [41]. On the other hand, $LaAlO_3$ is also susceptible for doping in both *A*- and *B*-site [39,41−43], thus enabling the formation of stabilized structures up to more than 1600 °C, with lower thermal conductivity [44], and improved the mechanical properties [45].

In this study, we evaluate $LaAlO_3$, as the first member in LA-based series of perovskite based materials with tailored TC properties, against standardized testing for TC materials.

2 Experimental

2.1 Preparation of $LaAlO_3$

$LaAlO_3$ (LA) powder was synthesized based on a citrate-precursor technique described in Ref. [46]. $La(NO_3)_3.6H_2O$ and $Al(NO_3)_3.9H_2O$ from Sigma Aldrich were used as La and Al sources. An aqueous solution of 0.407 mol/L in $La(NO_3)_3.6H_2O$ and 0.407 mol/L in $Al(NO_3)_3{\cdot}6H_2O$ was formed and citric acid was added to a molar ratio of La:Al:citric acid =1:1:4.5. Then, NH_4OH was added to 9<pH<10 and heated to 90 °C, while stirring. The formed gel was charred into a powder after firing at 350 °C for 1 h. This powder was finally annealed at 1100 °C for 2 h to produce LA. LA powder size was reduced by wet ball milling using zirconia grinding balls. The final particle size distribution of LA powder is given in supplementary material.

Pellets were formed by means of uniaxial pressing the LA powder under 74 MPa. Green pellet diameter was 13.0 mm, height was 3.5 mm unless specified differently, and the bulk density was 3.05 g/cm^3. Pellets were sintered at various temperatures in the range of 1200−1500 °C for 2 h.

YSZ (5%, mole fraction) by LTC Ltd, Korea, was also used for shaping specimens for mechanical properties comparison testing.

2.2 Material characterization

Phase formation was confirmed using a Siemens D600 XRD system employing Cu K_α radiation. The particle size was checked by laser particle size analysis using a Malvern 2000 Mastersizer. Viscosity of the solution precursor was measured using the Brookfield, DV-II-Pro viscometer at temperatures of (21.0±0.5) °C. Apparent porosity was measured utilizing the Archimedes method and following the respective standard method [47]. Bulk density of pellets was calculated as the mass of the dry pellet over the apparent volume of the pellet, based on the geometrical characteristics of the pellet.

IR spectra of samples were recorded by IR Fourier spectrometer BRUKER ALPHA equipped with diamond ATR accessory using single-beam optical scheme. Spectra were obtained within the range of 400−800 cm^{-1} with resolution of 4 cm^{-1}.

2.3 Thermal conductivity measurements

Thermal conductivity measurements were performed by means of the flash laser method, using a Netzsch LFA 457 MicroFlash instrument and samples as pellets with 8 mm in diameter and 3−4 mm in thickness. The temperatures were 25 and 750 °C in Ar atmosphere. The Nd-laser had pulse duration of 0.3 ms and a maximum energy of 18 J. The result of the measurement is the thermal diffusivity (D_{th} in mm^2/s) which has to be transformed to the thermal conductivity (λ in W/(m·K)) using the following equation:

$$\lambda(T)=D_{th}(T)\cdot\rho\cdot c_p \quad (1)$$

where ρ is the sample density in g/cm^3 and c_p is the specific heat capacity in J/(g·K).

For the $LaAlO_3$ samples, ρ=5.54 g/cm^3 and c_p= 0.427 J/(g·K) were used.

2.4 Mechanical testing

Basic mechanical and fracture properties of LA were measured using a high temperature mechanical test facility and indentation method, respectively. These data are required for the qualitative comparison of the LA properties with other top coat materials as well as input to numerical modelling of thermal barrier coatings to simulate the behaviour under service loading conditions and predicting life of the coatings.

Modulus, the stress−strain response and the ultimate strength of the LA samples in compression mode as a function of temperature were measured.

The high temperature mechanical test facility consists of a furnace that splits vertically along its center line and has a maximum continuous operating temperature of 1300 °C. The furnace has a relatively large internal void of 200 mm × 200 mm × 200 mm. A constant temperature within the furnace is achieved through a three-zone heating using six silicon carbide heating elements, each with independent control system to maintain the target temperature.

For the mechanical testing the furnace was mounted on a DARTEC 100 kN servohydraulic test machine. Water cooled aluminum loading bar fixtures are used at the top and bottom furnace entry points to ensure thermal isolation of the 99.7% alumina loading rods (L=400 mm; d=46 mm) from the test machine and the load cell. A self-aligning rotary ball joint fixture is included in the load line to ensure accurate fixture alignment.

Test specimens in the form of pellets are placed centrally between the parallel ends of the alumina loading rods before conditioning at test temperature prior to mechanical loading. The load and crosshead displacement are monitored during the test, with machine stiffness being compensated during post test data analysis.

Tests were performed in sintered pellets (see section 2.1) with diameter of 10 mm and height of 12 mm.

It must be noted that the sintering process produces samples with high level of consolidation and low levels of porosity compared with the top coats on the TBC are deposited using different spraying techniques which in generally results in lower level of consolidation and higher porosity.

The fracture toughness data from the cylindrical top coat LA samples were measured using the indentation method. There are several equations available in Refs. [48−50] for calculating the fracture toughness (K_{IC}) from micro-hardness tests. In this work, a variant of Lawn's equation [51] has been employed using the Vickers hardness indenter using the following equation:

$$K_{IC}=0.2038H_V a^{1/2}\left(\frac{c}{a}\right)^{-1.5} \quad (2)$$

where a is the half length of the indentation diagonal; c is the half length of the crack generated by indentation; H_V is Vickers hardness; K_{IC} is fracture toughness.

2.5 Spark plasma sintering

Spark plasma sintering (SPS) experiments were carried out on the Dr Sinter 515S Syntex apparatus. The powders were poured into a carbon die with 8 mm in diameter, the internal face of which was covered with a thin graphite foil (papayex@), to avoid direct contact between the powder and the graphite die. The die was closed by carbon punches at both sides that are used as current contacts, as well as to apply uniaxial pressure. DC pulses were delivered to the die by the punches allowing the temperature of the die to rise rapidly. Graphite felt around the die was also used to reduce the

heat loss by radiation. Sintering temperature was measured by an optical pyrometer focused on a small hole in the graphite die. For the maximum reproducibility, the sintering temperature and pressure were controlled by automatic controller units. The samples were heated by applying pulsed direct current which passes through punch and die system. The pulse time was set as 3.3 ms, a pulse pattern consisted of 12 pulses each followed by a period of 6.6 ms during which no current was used. All experiments were conducted in vacuum of about 0.1 Pa.

In all cases, the temperature was first raised to 600 °C within 1 min and a dwell time of 6 min was set to let time to monitor and regulate the temperature using the IR pyrometer. As soon as the temperature of 600 °C was reached, a constant uniaxial pressure of 100 MPa was applied to the die. Different experimental conditions were tested to optimize the sintering of LA. Samples were heated to a holding temperature (T) within 1 min; consequently, various heating rates of 500, 600, 700 and 800 (°)/min respectively for 1100, 1200, 1300 and 1400 °C have been applied. The sample was maintained at this temperature for 15 min. A rapid cooling, during which the pressure was decreased, ended the sintering cycle. In order to evaluate the sintering behavior of $LaAlO_3$ powder, a dilatometric study was performed using the SPS apparatus.

3 Results and discussion

3.1 Powder structural characterization

The particle size distribution of the LA powder after 60 h of ball milling is shown in Fig. 1(b). The powder exhibits a $D_{0.5}$ equal to 1.2 μm.

Figure 2 shows the XRD patterns of the powder received after different annealing temperatures, from 700 to 1100 °C. Single phase perovskite structure was confirmed at 1100 °C.

The ATR-IR spectra of the as-prepared powder are presented in Fig. 3. The dominating band is asymmetric and located at ca. 650 cm^{-1}. Based on previous studies regarding the optical properties of LA [52], this is the result from two primary peaks at 692 cm^{-1} and 652 cm^{-1}. A smaller band at ca. 556 cm^{-1} is also recorded. These, namely, three bands, correspond to the formation of AlO_6 octahedra [46,53]. One small band at ca. 495 cm^{-1} is also expected [52], whereas we record another at 406 cm^{-1}.

The deconvolution of the spectrum is also shown in Fig. 3. Four Lorentz oscillators were used and fitted to the measured spectrum. The fitted parameters, i.e., peak center (x_c), peak width (w) and peak area (A) are also presented in Fig. 3 [54,55]. The positions of the Lorentz oscillators, as well as the comparably larger

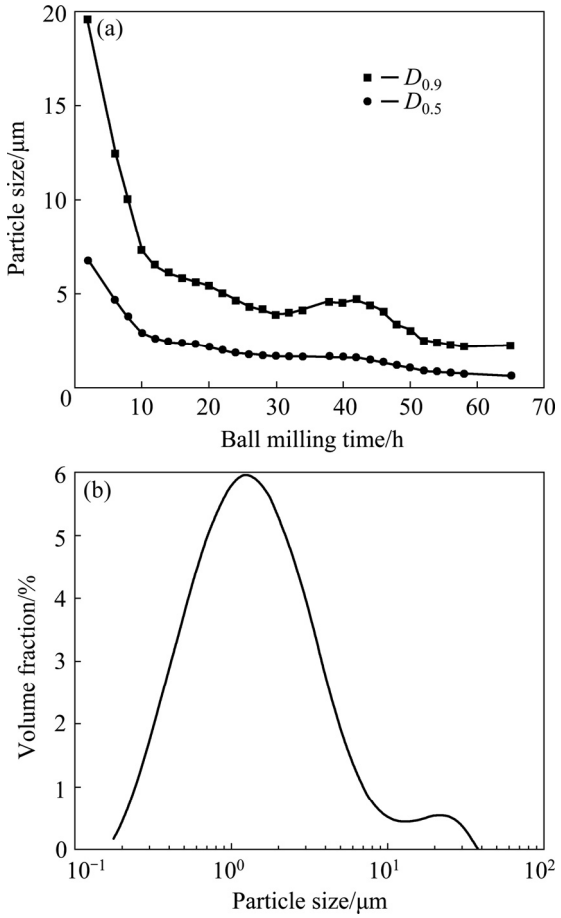

Fig. 1 Variation of $D_{0.5}$ and $D_{0.9}$ against ball milling time (a) and particle size distribution of LA powder after 60 h of ball milling (b)

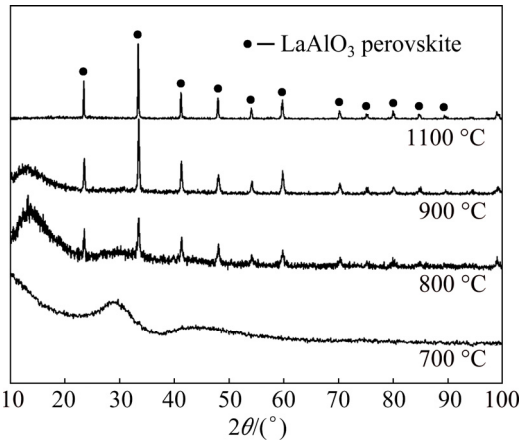

Fig. 2 XRD patterns of LA powder at different annealing temperatures

width of the oscillator at 691 cm^{-1}, are in accordance to pertaining the tabulated values [52].

3.2 Porosity and sintering

Porosity properties of the LA samples are summarized in Table 1.

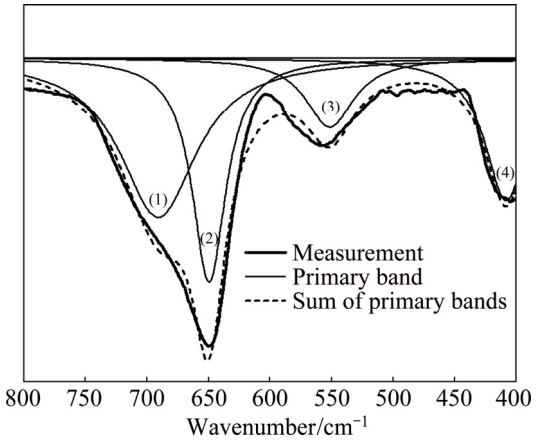

Parameter	Value	Error
$x_c(1)$/cm^{-1}	690.85	1.07
$w(1)$	76.16	3.08
$A(1)$	4531.39	269.92
$x_c(2)$/cm^{-1}	649.57	0.25
$w(2)$	33.16	1.06
$A(2)$	2791.77	134.74
$x_c(3)$/cm^{-1}	551.37	0.69
$w(3)$	47.49	2.72
$A(3)$	1236.71	73.75
$x_c(4)$/cm^{-1}	407.94	0.64
$w(4)$	42.20	2.04
$A(4)$	2250.47	120.52

Fig. 3 Deconvolution of ATR-IR spectra of $LaAlO_3$ powder after firing solution precursor at 350 °C and then annealed at 1100 °C (as prepared)

Table 1 Effect of conventional sintering temperature on pellet diameter, height, bulk density and porosity

Sintering temperature/ °C	Pellet diameter after sintering/ mm	Height of pellet after sintering/ mm	Bulk density/ (g·cm^{-3})	Open porosity/ %
1200	12.75	3.45	3.21	47.5
1300	11.50	3.20	4.26	34.4
1400	10.50	3.00	5.47	14.7
1500	10.25	2.95	5.81	1.8

The XRD patterns of the pellets sintered at 1200 °C and 1500 °C are presented in Figs. 4(b) and (c) respectively, for comparison to the respective pattern of the as-prepared powder. No changes are recorded compared with the starting powder, thus indicating a phase stability of the $LaAlO_3$ structures at these temperatures for the time studied.

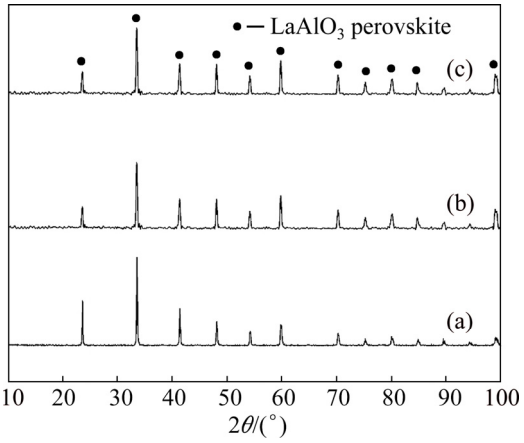

Fig. 4 XRD patterns of LA powder annealed at 1100 °C (as-prepared) (a), LA pellet sintered at 1200 °C for 2 h (b) and sintered at 1500 °C for 2 h (c)

Even though the $LaAlO_3$ structure is stable within these sintering conditions, a substantial sintering is recorded. Open porosity is reduced from 47.5% to virtually zero, and bulk density is increased from 3.21 to 5.81 g/cm^3 as the sintering temperature increases from 1200 to 1500 °C. Single crystal *R*3*c* LA specimens exhibit density of 6.51 g/cm^3.

Additional densification experiments have been performed by means of SPS. For producing fully dense LA ceramics, four sintering processes were tested. The temperature and pressure profiles are presented in Fig. 5.

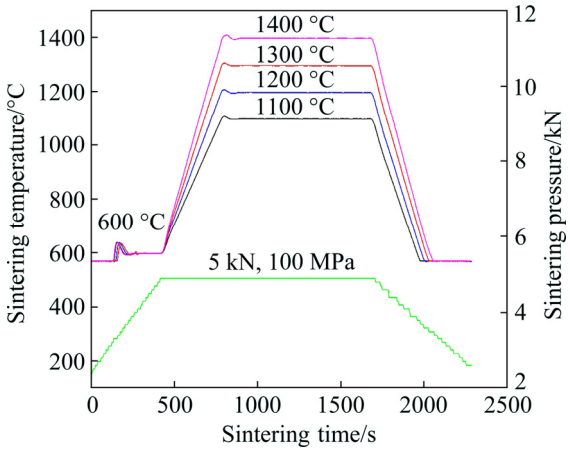

Fig. 5 SPS sintering temperature and sintering pressure profiles versus sintering time

Typical curves of sintering displacement rate z vs time corresponding to the inverse of the shrinkage curves vs time and the displacement (dz/dt versus time) curves for four different holding temperatures are presented in Figs. 6(a) and (b), respectively. These curves illustrate the densification and densification rate of the four samples. These curves have been plotted from 400 to 1800 s to ensure that the observed shrinkage is not due to

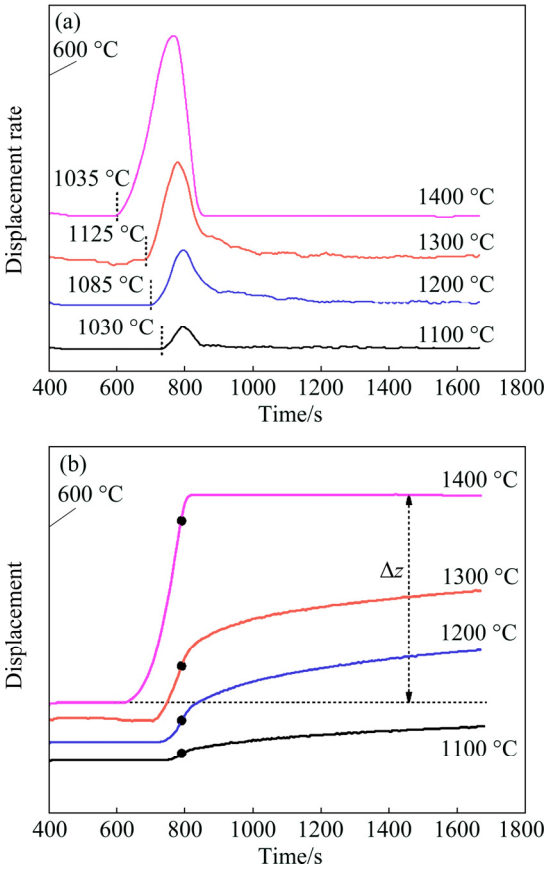

Fig. 6 SPS sintering displacement rate (a) and SPS sintering displacement versus sintering time at different holding temperatures (b) (The black points correspond to the displacement at the scheduled holding temperature)

the application of a higher pressure (below 400 s) and assuming that during sample cooling (up to 1700 s) sintering no longer takes place and therefore the cooling shrinkage is only dependent on the thermal dilatation. The dilatometric curves are very similar. Up to 400 s, i.e. 600 °C, the displacement is first of all constant and at a certain time, corresponding to a given temperature, the displacement increases indicating that the sintering process begins and the material starts to shrink. As long as the temperature increases the thermal dilatation continues as well. During the dwell time at the sintering temperature, the thermal dilatation is stopped, but shrinkage caused by the sintering process continues until the end of the plateau excepted for 1400 °C where the shrinkage remains constant after a holding time of 15 s. Figure 6(b) indicates that the total shrinkage Δz increases linearly with the holding temperature or heating rate as can be seen in Fig. 7, where Δz versus dwelling temperatures and heating rates are plotted.

Moreover, it can be observed on the densification rate vs time curves that the higher the holding temperature, the earlier the densification starts. By using the same mass for each sample, and the same heating rate to reach the scheduled holding temperature, for a same powder, the densification normally starts at the same temperature. It is not the case here due to the different heating rates used to reach the desired temperature of the plateau as can be seen in Fig. 6(b).

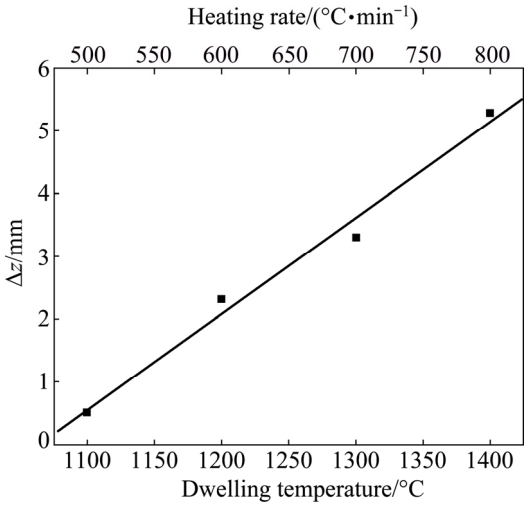

Fig. 7 Plot of Δz versus dwelling temperature and heating rate

To get fully dense samples by SPS, a plateau at 1400 °C for 15 s is enough. Results are in good agreement with conventional sintering approach (Table 1). Heating the samples longer or at higher temperature would lead to modification of their microstructure, e.g., grain growth.

In a typical dilatometry curve of LA pellet sintered at 1500 °C at 550−600 °C, a change in the slope is recorded, as illustrated by the straight red line (Fig. 8). This change in the dilatation variation is related to the phase transition temperature of LA, from the rhombohedral (*R*3*c*) to the ideal cubic (*Pm*3*m*) [38].

This change in the coefficient of thermal expansion (CTE) is however small. As depicted in Fig. 8(a), the linear model follows fairly well the experimental data (R^2=0.99946) from ΔT=200 °C to ΔT=1350 °C, and yields a CTE of $(5.480\pm0.002)\times10^{-6}$ K^{-1}. In Fig. 8(b) two different linear models were applied; the first from 200 to 600 °C and the second from 900 to 1350 °C. Based on the regression analysis the CTE for temperatures up to 600 °C is 5.69×10^{-6} K^{-1}, while for temperatures higher than 900 °C the CTE is 5.68×10^{-6} K^{-1}, thus illustrating the negligibility of the CTE change upon phase transformation.

In dilatometric results of LA pellets sintered at a lower temperature of 1200 °C, a similar but more intense change in the $\Delta L/L_0$ vs ΔT slope is observed (L_0 is original length, ΔL is length change of specimen). CTE is calculated for the two segments of the dilatometric measurement. At 200−500 °C, the CTE is calculated to be 5.43×10^{-6} K^{-1} while for temperatures higher than 650 °C and up to 1050 °C the CTE is 4.81×10^{-6} K^{-1},

which corresponds to a decrease of ca. 11%. This change in CTE is gradually decreased after the second treatment to 1200 °C and the CTE varies from 5.76×10^{-6} K^{-1} to 5.30×10^{-6} K^{-1}, corresponding to a change of ca. 8%.

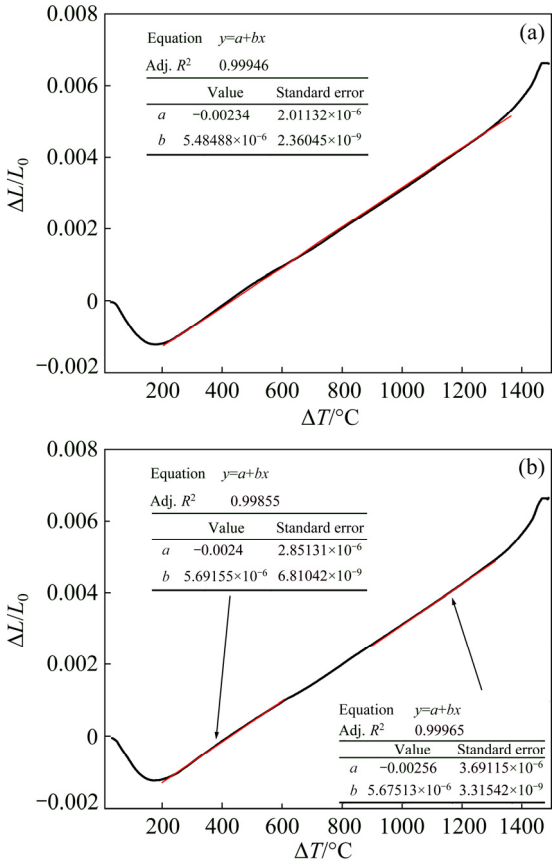

Fig. 8 Typical calculations of CTE for $LaAlO_3$ pellet sintered at 1500 °C using one linear model throughout measured ΔT (a), and using two different linear models below and above phase transition temperature (b)

The dilatometric measurements of the pellet sintered at 1200 °C and heated up to 1200 °C for two, three and four time are also calculated and given in Tables 2 and 3. All changes in CTE below 500 °C and above 650 °C are shown in Table 2. The calculated values of CTE are 5.21×10^{-6}, 5.20×10^{-6} and 5.25×10^{-6} K^{-1}, respectively, with the linear model fitting being fairly well in all cases (Table 3).

In the case of a pellet sintered at 1200 °C and undergone the thermal process described before (4 times heated up to 1200 °C) when during measurement was heated up to 1500 °C, the CTE within the same temperature range as before is calculated to be 5.25×10^{-6} K^{-1}, with the linear model fitting well (R^2=0.99954). All the calculated CTE values (Table 3), illustrate a stability in CTE for temperatures up to 1200 °C. For ΔT higher than 1200 °C, which corresponds to ~1300 °C, the pellet undergoes significant shrinkage. This is shown in Fig. 9 and is discussed hereafter.

Table 2 Change of CTE below 500 °C and above 650 °C

Sintering temperature/°C	CTE below 500 °C/10^{-6} K^{-1}	CTE above 600 °C/10^{-6} K^{-1}	CTE change/%
1500	5.69	5.68	0.18
1200 (1st run)	5.43	4.81	11
1200 (2nd run)	5.76	5.30	8
1200 (3rd run)	5.10	5.39	4
1200 (4th run)	5.10	5.41	6

Table 3 Calculated CTE of pellets, using one linear model through dilatometric data

Sintering temperature/°C	CTE/10^{-6} K^{-1}	R^2
1500	5.49	0.99946
1200 (1st run)	4.72	0.99869
1200 (2nd run)	5.21	0.99932
1200 (3rd run)	5.20	0.99923
1200 (4th run)	5.25	0.99909
1200 (up to 1500 °C)	5.25	0.99954
1200 (up to 1500 °C, 2nd run)	6.35	0.99961

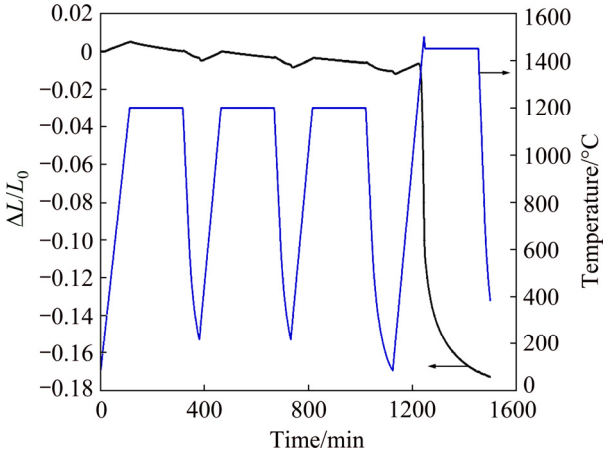

Fig. 9 Thermal process and dilatometric profiles of $LaAlO_3$ pellet sintered at 1200 °C for 2 h

However, the pellet undergoes shrinkage during thermal treatment up to 1200 °C. As shown in Fig. 9 at the end of the third thermal cycle which is located at ~1125 min, $\Delta L/L_0$ is −0.011 compared with the initial value. For this particular sample, L_0 was 11.293 mm, therefore the absolute shrinkage was ΔL=−0.124 mm. For temperatures higher than 1300 °C, the shrinkage increases.

3.3 Thermal stability

Pellets prepared according to the procedure described before were treated for 300 h at 1300 °C to assess the thermal stability of the synthesized material. XRD patterns were identical, thus indicating increased structural thermal stability.

3.4 Thermal conductivity

Thermal conductivity increases with increasing sintering temperature as seen in Fig. 10 and Table 4. Increasing the sintering temperature results in porosity decrease; the density of the samples is increasing and with it, its ability to conduct thermal energy. This indicates that a specific material processing will be necessary in order to achieve a controllable, but also persistent at elevated temperatures porosity of the applied layers and so to reduce the thermal conductivity. For example, functionally graded design of LA-containing composites can lead to controllable porosity and reduce the thermal conductivity [19].

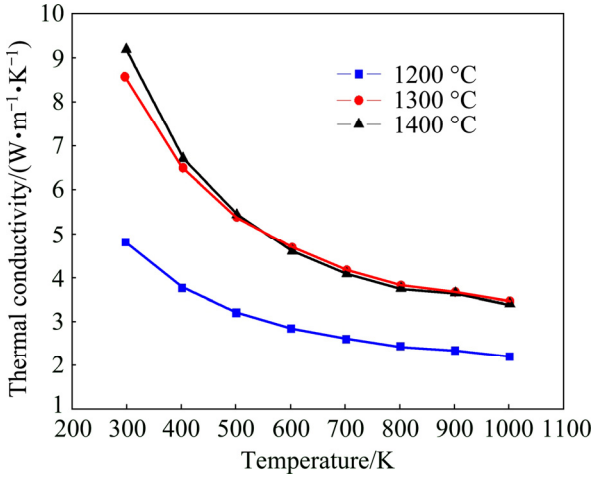

Fig. 10 Thermal conductivity of LA sintered at 1200, 1300 and 1400 °C

Table 4 Thermal conductivity (λ) of LA sintered at different temperatures

Sintering temperature/°C	D_{th}/(mm^2·s^{-1})	λ/(W·m·K^{-1})
1400	9.190±0.057	3.408±0.007
1300	8.568±0.076	3.430±0.016
1200	4.807±0.037	2.198±0.012

D_{th} at 298 K; λ at 1000 K

3.5 Mechanical properties

Results in terms of the measured engineering stress−strain curves obtained from the compression tests performed at 1000, 1200 and 1300 °C on pellets of LA samples are shown in Fig. 11.

The measured elastic moduli and ultimate stresses as a function of temperatures are shown in Fig. 12, along with the results obtained from the YSZ samples for comparison.

Elastic modulus of LA decreases from 63 GPa to 25 GPa, when the temperature increases from 1000 to 1300 °C. Similar behavior is recorded also for YSZ samples prepared by similar conditions using LTC Ltd. powder.

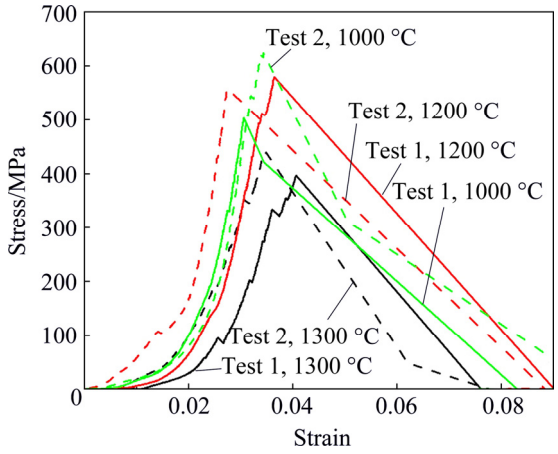

Fig. 11 Measured strain−stress curves for LA sintered at different temperatures

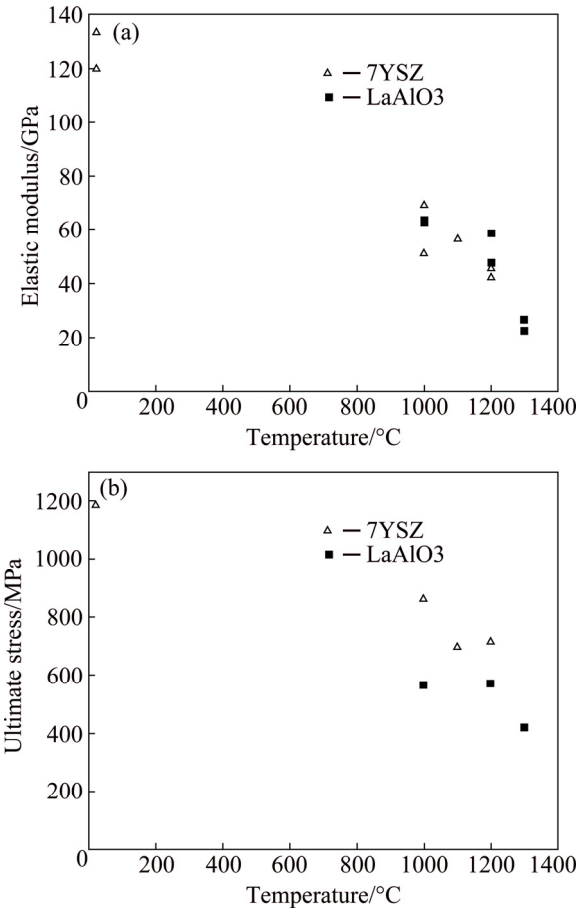

Fig. 12 Elastic modulus and ultimate stress of $LaAlO_3$ sintered at different temperatures

The ultimate stress of LA is 590 MPa, which remains virtually unaffected with temperature in the range of 1000−1200 °C and decreases to 430 MPa, at 1300 °C. In the range of 1000−1200 °C YSZ ultimate stress is decreased from 850 to 700 MPa.

Typical cracks obtained from the indentation tests on cylinders are shown in Fig. 13. The calculated K_{IC} values for LA are given in Table 5. Respective

measurements were also performed on YSZ cylindrical samples which are given in Table 5 for comparison.

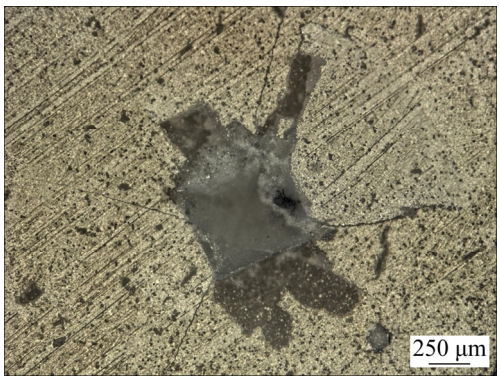

Fig. 13 Typical cracks from indentation tests

Table 5 K_{IC} measurements for $LaAlO_3$

Material	Specimen type	K_{IC}/(MPa·m$^{1/2}$)
7YSZ	Cylinder	7.03, 4.16, 5.57
LaAlO3	Cylinder	3.37, 3.19, 2.90

4 Conclusions

1) We evaluated the properties of basic perovskite compound $LaAlO_3$ in the context of YSZ replacement in TBCs. $LaAlO_3$ properties as in all perovskites can be tailored via *A*- or *B*- site substitution by a vast number of periodic table elements. The $LaAlO_3$ perovskite structure was confirmed by means of XRD and ATR-IR. SPS and conventional sintering studies from 1200 to 1500 °C revealed a significant densification from 3.21 to 5.81 g/cm^3 indicating that material annealing should be made at least at 1400 °C. Under this condition CTE studies showed negligible dimensional change in phase transition temperature of LA, from the rhombohedral (*R*3*c*) to the ideal cubic (*Pm*3*m*). As the thermal conductivity increases with increasing sintering temperature and thus higher densities, one has to pay attention to avoid dense LA layers in order to improve its ability to act as a functional thermal barrier coating.

2) Experimentally measured material properties in terms of both the static strength and the fracture toughness of the LA and the YSZ were reported. The experimental setup developed as part of this work has successfully been used to measure the ultimate stress and the elastic modulus at elevated temperatures of up to 1300 °C.

3) The elastic moduli were measured to be 63.07, 52.98 and 24.70 GPa at 1000, 1200 and 1300 °C, respectively. The mechanical properties of the LA are very similar to the YSZ. However, the average fracture toughness value for $LaAlO_3$ is found to be 3.15 MPa·m$^{1/2}$ which is lower than the corresponding average value for the YSZ of 5.59 MPa·m$^{1/2}$.

4) The data reported here are very important not only for comparing the mechanical and fracture behaviour of different TBCs developed involving $LaAlO_3$ but are also essential for input into numerical simulations using finite element techniques for predicting the response and the life of the TBCs under service conditions. Despite how useful such properties can be it is expected that material features and performance will be greatly affected by microstructural effects introduced in the thermal spraying coating fabrication process.

Acknowledgements

Financial support by THEBARCODE-Development of Multifunctional Thermal Barrier Coatings and Modeling Tools for High Temperature Power Generation with Improved Efficiency FP7-NMP-2012-SMALL-6, Collaborative project and by MATENERGY project of Technological Educational Institute of Sterea Ellada.

References

[1] VASSEN R, JARLIGO M, STEINKE T, MACK D, STÖVER D. Overview on advanced thermal barrier coatings [J]. Surface and Coatings Technology, 2010, 205: 938−942.

[2] PADTURE N, GELL M, JORDAN E. Thermal barrier coatings for gas-turbine engine applications [J]. Science, 2002, 296: 280−284.

[3] CLARKE D, OECHSNER M, PADTURE N. Thermal-barrier coatings for more efficient gas-turbine engines [J]. MRS Bulletin, 2012, 37: 891−898.

[4] XU H, GUO H. Thermal barrier coatings [M]. 1st ed. Cambridge: Elsevier Science, 2011.

[5] DAROONPARVAR M, YAJID M A M, YUSOF N M, FARAHANY S, HUSSAIN M S, BAKHSHESHI-RAD H R, VALEFI Z, ABDOLAHI A. Improvement of thermally grown oxide layer in thermal barrier coating systems with nano alumina as third layer [J]. Transactions of Nonferrous Metals Society of China 2013, 23: 1322−1333.

[6] LU Z, KIM M S, MYOUNG S W, LEE J H, JUNG Y G, KIM I S, JO C Y. Thermal stability and mechanical properties of thick thermal barrier coatings with vertical type cracks [J]. Transactions of Nonferrous Metals Society of China 2014, 24: 29−35.

[7] STECURA S. Effects of compositional changes on the performance of a thermal barrier coating system [C]//Third Annual Conference on Composites and Advanced Materials. Florida, Cleveland Ohio, 1979: E9751−E9775

[8] CHEVALIER J, GREMILLARD L, VIRKAR A, CLARKE D. The tetragonal-monoclinic transformation in zirconia: Lessons learned and future trends [J]. Journal of the American Ceramic Society, 2009, 92: 1901−1920.

[9] MERCER C, WILLIAMS J, CLARKE D, EVANS A. On a ferroelastic mechanism governing the toughness of metastable tetragonal-prime (t′) yttria-stabilized zirconia [J]. Proceedings of the Royal Society A: Mathematical, Physical and Engineering Sciences, 2007, 463: 1393−1408.

[10] CLARKE D, LEVI C. Materials design for the next generation thermal barrier coatings [J]. Annual Review of Materials Research, 2003, 33: 383−417.

[11] MAUER G, JARLIGO M, MACK D, VASSEN R. Plasma-sprayed thermal barrier coatings: New materials, processing issues, and solutions [J]. Journal of Thermal Spray Technology, 2013, 22: 646−658.

[12] QU Z, CHENG X, WU J, HE R, PEI Y, FANG D. An investigation on erosion behavior of nanostructured 7YSZ coatings at elevated temperature [J]. Surface and Coatings Technology, 2016, 299: 129−134.

[13] RAMACHANDRAN C, BALASUBRAMANIAN V, ANANTHAPADMANABHAN P, VISWABASKARAN V. Influence of the intermixed interfacial layers on the thermal cycling behaviour of atmospheric plasma sprayed lanthanum zirconate based coatings [J]. Ceramics International, 2012, 38: 4081−4096.

[14] DI GIROLAMO G, MARRA F, BLASI C, SCHIOPPA M, PULCI G, SERRA E, VALENTE T. High-temperature mechanical behavior of plasma sprayed lanthanum zirconate coatings [J]. Ceramics International, 2014, 40: 11433−11436.

[15] ZHOU H, LI F, HE B, WANG J, SUN B D. Nanostructured yttria stabilized zirconia coatings deposited by air plasma spraying [J]. Transactions of Nonferrous Metals Society of China 2007, 17: 389−393.

[16] VASSEN R, CAO X, TIETZ F, BASU D, STOVER D. Zirconates as new materials for thermal barrier coatings [J]. Journal of American Ceramic Society, 2000, 83: 2023−2028.

[17] MA W, MACK D, VASSEN R, STÖVER D. Perovskite-type strontium zirconate as a new material for thermal barrier coatings [J]. Journal of the American Ceramic Society, 2008, 91: 2630−2635.

[18] MA W, JARLIGO M, MACK D, PITZER D, MALZBENDER J, VASSEN R, STÖVER D. New generation perovskite thermal barrier coating materials [J]. Journal of Thermal Spray Technology, 2008, 17: 831−837.

[19] GARCIA E, CANO C, COYLE T, OSENDI M, MIRANZO P. Thermally sprayed $CaZrO_3$ coatings [J]. Journal of Thermal Spray Technology, 2008, 17: 865−871.

[20] VASSEN R, DOERING J, DIETRICH M, LEHMANN H, STOEVER D. Recent developments in the field of plasma-sprayed thermal barrier coatings [C]//Proceedings of the International Gas Turbine Congress. Tokyo, TS-129, 2003: 1−9.

[21] KWON J, JUNG S, LEE S, LEE P, LEE J, JUNG Y, PAIK U, CHO H, CHANG J. Interfacial stability and contact damage resistance by incorporating buffer layer in thermal barrier coatings [J]. Progress in Organic Coatings, 2010, 68: 135−141.

[22] STATHOPOULOS V, SADYKOV V, PAVLOVA S, BESPALKO Y, FEDOROVA Y, BOBROVA L, SALANOV A, ISHCHENKO A, STOYANOVSKY V, LARINA T, ULIANITSKY V, VINOKUROV Z, KRIVENTSOV V. Design of functionally graded multilayer thermal barrier coatings for gas turbine application [J]. Surface and Coatings Technology, 2016, 295: 20−28.

[23] COSTA C, STATHOPOULOS V, BELESSI V, EFSTATHIOU A. An investigation of the $NO/H_2/O_2$ (Lean-deNOx) reaction on a highly active and selective $Pt/La_{0.5}Ce_{0.5}MnO_3$ catalyst [J]. Journal of Catalysis 2001, 197: 350−364.

[24] STATHOPOULOS V, BELESSI V, LADAVOS A. Samarium based high surface area perovskite type oxides $SmFe_{1-X}AlXO_3$ (X=0.00, 0.50, 0.95). Part II, Catalytic combustion of CH_4 [J] Reaction Kinetics and Catalysis Letters, 2001, 72: 49−55.

[25] STATHOPOULOS V, BELESSI V, LADAVOS A. Samarium based high surface area perovskite type oxides $SmFe_{1-X}AlXO_3$ (X=0.00, 0.50, 0.95). Part I, Synthesis and characterization of materials [J]. Reaction Kinetics and Catalysis Letters, 2001, 72: 43−48.

[26] COSTA C, SAVVA P, ANDRONIKOU C, LAMBROU P, POLYCHRONOPOULOU K, BELESSI V, STATHOPOULOS V, POMONIS P, EFSTATHIOU A. An Investigation of the $NO/H_2/O_2$ (Lean De-NO*x*) reaction on a highly active and selective $Pt/La_{0.7}Sr_{0.2}Ce_{0.1}FeO_3$ catalyst at low temperatures [J]. Journal of Catalysis, 2002, 209: 456−471.

[27] STATHOPOULOS V, BELESSI V, BAKAS T, NEOPHYTIDES S, COSTA C, POMONIS P, EFSTATHIOU A. Comparative study of La−Sr−Fe−O perovskite-type oxides prepared by ceramic and surfactant methods over the CH_4 and H_2 lean-deNO*x* [J]. Applied Catalysis B: Environmental, 2009, 93: 1−11.

[28] GASPARYAN H, ARGIRUSIS C, SZEPANSKI C, SOURKOUNI G, STATHOPOULOS V, KHARLAMOVA T, SADYKOV V, BEBELIS S. Electrochemical characterization of a $La_{0.8}Sr_{0.2}Ni_{0.4}Fe_{0.6}O_{3-\delta}$ electrode interfaced with $La_{9.83}Si_5Al_{0.75}Fe_{0.25}O_{26\pm\delta}$ apatite-type electrolyte [J]. ECS Transactions, 2009, 25: 2681−2688.

[29] JARLIGO M, MACK D, VASSEN R, STÖVER D. Application of plasma-sprayed complex perovskites as thermal barrier coatings [J]. Journal of Thermal Spray Technology, 2009, 18: 187−193.

[30] JARLIGO M, MAUER G, SEBOLD D, MACK D, VASSEN R, STÖVER V. Decomposition of $Ba(Mg_{1/3}Ta_{2/3})O_3$ perovskite during atmospheric plasma spraying [J]. Surface and Coatings Technology, 2012, 206: 2515−2520.

[31] FU F, DAROLIA R, GORMAN M, NAGARAJ B. Thermal barrier coating systems including a rare earth aluminate layer for improved resistance to CMAS infiltration and coated articles: US patent, US8062759 B2 [P]. 2011-11-22.

[32] SUBRAMANIAN R, SABOL S, GOEDJEN J, SLOAN K, VANCE S, Thermal barrier coatings for turbine components: US patent, US6365281 B1 [P]. 2002-04-02.

[33] GADOW R, LISCHKA M. Lanthanum hexaaluminate−novel thermal barrier coatings for gas turbine applications−materials and process development [J]. Surface and Coatings Technology, 2002, 151−152: 392−399.

[34] CHEN X, ZHAO Y, HUANG W, MA H, ZOU B, WANG Y, CAO X. Thermal aging behavior of plasma sprayed LaMgAl11O19 thermal barrier coating [J]. Journal of the European Ceramic Society, 2011, 31: 2285−2294.

[35] CAO X, VASSEN R, JUNGEN W, SCHWARTZ S, TIETZ F, STÖVER D. Thermal stability of lanthanum zirconate plasma-sprayed coating [J]. Journal of the American Ceramic Society, 2001, 84: 2086−2090.

[36] WANG Y, XIAO P. The phase stability and toughening effect of 3Y-TZP dispersed in the lanthanum zirconate ceramics [J]. Materials Science and Engineering A, 2014, 604: 34−39.

[37] SCHAPER H, DOESBURG E, van REIJEN L. The influence of lanthanum oxide on the thermal stability of gamma alumina catalyst supports [J]. Applied Catalysis, 1983, 7: 211−220.

[38] LUO X, WANG B, Structural and elastic properties of LaAlO3 from first-principles calculations [J]. Journal of Applied Physics, 2008, 104: 63−68.

[39] INABA H, HAYASHI H, SUZUKI M. Structural phase transition of perovskite oxides $LaMO_3$ and $La_{0.9}Sr_{0.1}MO_3$ with different size of B-site ions [J]. Solid State Ionics, 2001, 144: 99−108.

[40] WANG J, ISHIZAWA N, YE X. Phase transition and thermal expansion of the LaAlO3 single crystal at high temperatures [J]. Journal of Alloys and Compounds, 2014, 594: 23−26.

[41] VASYLECHKO L, SENYSHYN A, BISMAYER U. Perovskite- type aluminates and gallates [M]//Handbook on the Physics and Chemistry of Rare Earths. Vol.39. Netherlands North-Holland: Elsevier, 2009: 113−295.

[42] FU Q, TIETZ F, LERSCH P, STÖVER D. Evaluation of Sr- and Mn-substituted $LaAlO_3$ as potential SOFC anode materials [J]. Solid State Ionics, 2006, 177: 1059−1069.

[43] CHEN T, FUNG K. *A* and *B*-site substitution of the solid electrolyte $LaGaO_3$ and $LaAlO_3$ with the alkaline-earth oxides MgO and SrO [J]. Journal of Alloys and Compounds, 2004, 368: 106−115.

[44] WAN C, QU Z, HE Y, LUAN D, PAN W. Ultralow thermal

conductivity in highly anion-defective aluminates [J]. Physical Review Letters, 2008, 101: 085901.

[45] JARLIGO M, MACK D, MAUER G, VASSEN R, STÖVER D. Atmospheric plasma spraying of high melting temperature complex perovskites for TBC application [J]. Journal of Thermal Spray Technology, 2009, 19: 303−310.

[46] YU H, WANG J, WANG S, KUO Y. Thermochemical behavior of metallic citrate precursors for the production of pure $LaAlO_3$ [J]. Journal of Physics and Chemistry of Solids, 2009, 70: 218−223.

[47] ASTM C373−88(2006), Standard Test Method for Water Absorption, Bulk Density, Apparent Porosity, and Apparent Specific Gravity of Fired Whiteware Products [S]. ASTM International, West Conshohocken, PA, DOI: 10.1520/C0373 88R06, 2006. (https://www.astm.org/ DATABASE. CART/ HISTORICAL/C373-88R06.htm)

[48] SPIEGLER R, SCHMAUDER S, SIGL L. Fracture toughness evaluation of WC−Co alloys by indentation testing [J] Journal of Hard Materials, 1990, 1: 147−158.

[49] KRUZIC J, KIM D, KOESTER K, RITCHIE R. Indentation techniques for evaluating the fracture toughness of biomaterials and hard tissues [J]. Journal of the Mechanical Behavior of Biomedical Materials, 2009, 2: 384−395.

[50] QUINN G, BRADT R. On the Vickers indentation fracture toughness test [J]. Journal of the American Ceramic Society, 2007, 90: 673−680.

[51] ROCHA-RANGEL E. Fracture toughness determinations by means of indentation fracture, nanocomposites with unique properties and applications in medicine and industry [M]. John Cuppoletti. InTech, DOI: 10.5772/18127, 2011.

[52] ZHANG Z, CHOI B, FLIK M, ANDERSON A. Infrared refractive indices of $LaAlO_3$, $LaGaO_3$, and $NdGaO_3$ [J]. Journal of Optical Society of America B, 1994, 11: 2252−2257.

[53] CHEN B, YU J, LIANG X. $LaAlO_3$ hollow spheres: Synthesis and luminescence properties [J]. Langmuir, 2011, 27: 11654−11659.

[54] GEORGIOPOULOS I, MARATHONITI E, VOURDAS N, ANDREOULI K, STATHOPOULOS V. Comparative study on liquid plasma sprayed lanthanum aluminate oxide coatings using different feedstock materials for potential TBC application [C]//25th Advanced Aerospace Materials and Processes (AeroMat) Conference and Exposition. Orlando, Florida, USA: ASM, 2014.

[55] MARATHONITI E, VOURDAS N, GEORGIOPOULOS I, TRUSCA O, TRUSCA I, ANDREOULI C, STATHOPOULOS V, Development of $LaAlO_3$-based thermal barrier coatings by solution precursor thermal spray [C]//International Conference on Material Technologies and Modeling-MMT. Ariel, Israel, 2014: 195−205.

$LaAlO_3$作为热障涂层顶级涂层材料的评价

N. VOURDAS[1], E. MARATHONITI[1], P. K. PANDIS[1],
Chr. ARGIRUSIS[2], G. SOURKOUNI[3], C. LEGROS[4], S. MIRZA[5], V. N. STATHOPOULOS[1]

1. Laboratory of Chemistry and Materials Technology, School of Technological Applications, Technological Educational Institute of Sterea Ellada, 34400 Psachna Campus, Evia, Greece;
2. School of Chemical Engineering, National Technical University of Athens, I. Polytechneiou 9, 15780 Zografou, Athens, Greece;
3. Inst. f. Metallurgie, Technische Universität Clausthal, Robert-Koch-Str. 42, 38678 Clausthal-Zellerfeld, Germany;
4. Institut de Chimie Moléculaire et des Materiaux d´Orsay, Université Paris Sud, Bât 410, 91405 Orsay Cedex, France;
5. ELEMENT S.A., Hitchin SG4 0TW, UK

摘　要：钙钛矿是一种多用途氧化物材料，可以通过调整成分而改变其性能以满足特定的需求。采用柠檬酸法制备 $LaAlO_3$，用 XRD 和 FT-IR 检测确认其钙钛矿结构，并评估其用于热障涂层(TBC)技术所需的性能。检测溶液前驱物的粘度并通过激光粒度仪分析其粒度。采用传统烧结和放电等离子烧结使材料致密化。用阿基米德法测试材料的表观孔隙率，并测试材料的导热系数和热膨胀系数。测试材料的高温(最高达 1300 °C)力学性能和断裂性能。结果表明，在 1200~1400 °C 烧结的样品，其热膨胀系数为$(5.5\sim6.5)\times10^{-6}$ K^{-1}，热导率为 2.2~3.4 W/(m·K)。在 1000~1300 °C 范围内测量弹性模量和极限应力，通过微压痕测算的断裂韧性约为 3 $MPa/m^{1/2}$。热处理温度从 1200 °C 提高到 1500 °C，材料发生明显致密化，密度从 3.21 g/cm^3 提高到 5.81 g/cm^3，表明材料热处理的最低温度应为 1400 °C。在相变温度下，$LaAlO_3$ 从菱方结构(*R*3*c*)转变为理想的立方结构(*Pm*3*m*)，而其晶格尺寸的变化可以忽略。本研究报道的数据可用于比较涉及 $LaAlO_3$ 的不同 TBC 的力学和断裂行为，也可用于数值模拟。

关键词：钙钛矿；铝化镧；热障涂层(TBC)

(Edited by Xiang-qun LI)